POLITECNICO DI TORINO
Repository ISTITUZIONALE

Nonlinear dynamics and band gap evolution of thin-walled metamaterial-like structures

Original
Nonlinear dynamics and band gap evolution of thin-walled metamaterial-like structures / Augello, R., Carrera, E.. - In: JOURNAL OF SOUND AND VIBRATION. - ISSN 0022-460X. - 578:(2024). [10.1016/j.jsv.2024.118329]

Availability:
This version is available at: 11583/3017464 since: 2026-11-03T12:05:21Z

Publisher:
Academic Press - Elsevier

Published
DOI:10.1016/j.jsv.2024.118329

Terms of use:

This article is made available under terms and conditions as specified in the corresponding bibliographic description in the repository

Publisher copyright

(Article begins on next page)

22 November 2026

Journal of Sound and Vibration 578 (2024) 118329

Contents lists available at ScienceDirect

Journal of Sound and Vibration

journal homepage: www.elsevier.com/locate/jsvi

Nonlinear dynamics and band gap evolution of thin-walled metamaterial-like structures

R. Augello [a,*,1], E. Carrera [a,b,2]

[a] Mul[2] Group, Department of Mechanical and Aerospace Engineering, Politecnico di Torino, Corso Duca degli Abruzzi 24, 10129 Torino, Italy
[b] Department of Mechanical Engineering, College of Engineering, Prince Mohammad Bin Fahd University, P.O. Box 1664, Al Khobar 31952, Kingdom of Saudi Arabia

ARTICLE INFO

Keywords:
Metamaterial
Band gap evolution
Nonlinear analysis
Carrera Unified Formulation

ABSTRACT

This paper explores the dynamic behavior of metamaterial-like structures by investigating the evolution of their band gap under the influence of geometrical nonlinearities in the large displacement/rotations field. The study employs a unified framework based on the Carrera Unified Formulation (CUF) and a total Lagrangian approach to develop higher-order one-dimensional beam theories that account for geometric nonlinearities. The axis discretization is achieved through a finite element approximation. The equations of motion are solved around nonlinear static equilibrium states, which are determined using a Newton–Raphson algorithm combined with a path-following method of arc-length type. The CUF approach introduces two key innovations that are highly suitable for the evolution of the band gap:

(1) Thin-walled structures can be effectively represented using a **single** one-dimensional beam model, overcoming the common limitations of standard finite elements. This is crucial as three-dimensional solid elements would result in significant computational costs, and two-dimensional elements based on von Kármán theory pose limitations for this type of investigation. Moreover, employing one-dimensional finite elements usually requires a combination of elements, leading to additional mathematical complexities in their connections and lacking geometric precision.

(2) CUF enables the use of the full Green–Lagrange strain tensor without the need for assumptions, as is the case with von Kármán nonlinearities. The paper specifically compares results obtained with linear and nonlinear stiffness matrices, highlighting the differences. Numerical investigations are conducted on thin-walled structures composed of repeatable cells, assessing mode changes under traction and compression loading. Additionally, the paper presents a more complex metamaterial-like structure. The findings emphasize that the band gap is an inherent property of the equilibrium state, underscoring the necessity of a proper nonlinear analysis for accurately evaluating frequency transitions.

1. Introduction

Metamaterials, initially proposed by Smith and Kroll [1] in the electromagnetic domain as locally resonant periodic materials, aim to create a 'left-handed' medium with negative electromagnetic permeability and permittivity, as originally conceptualized

* Corresponding author.
E-mail addresses: riccardo.augello@polito.it (R. Augello), erasmo.carrera@polito.it (E. Carrera).
[1] Postdoc.
[2] Full Professor of Aeronautics and Astronautics.

https://doi.org/10.1016/j.jsv.2024.118329
Received 8 December 2023; Received in revised form 29 January 2024; Accepted 2 February 2024
Available online 8 February 2024
0022-460X/© 2025 The Authors. Published by Elsevier Ltd. This is an open access article under the CC BY license (http://creativecommons.org/licenses/by/4.0/).

by Veselago [2]. The exploration of an analogy between acoustic and electromagnetic waves has spurred research in acoustic metamaterials [3], where density and bulk modulus serve as analogues for permeability and permittivity. These engineered materials, representing a groundbreaking class, deviate from natural properties and provide unprecedented control over wave propagation in both electromagnetic and acoustic realms. Unlike traditional materials with predictable behaviors constrained by natural limitations, metamaterials empower designers to customize specific responses to electromagnetic or acoustic stimuli. The prospect of achieving acoustic cloaking [4] and subwavelength acoustic lenses [5] is presented by introducing novel properties. This control is meticulously established by arranging subwavelength structures, thus the investigation of wave propagation and mode evolution in metamaterials has become a central focus of research, unlocking innovative possibilities in telecommunications, imaging, and sensing. Amid the diverse range of captivating phenomena associated with metamaterials, the notion of a band gap emerges as a pivotal element for comprehending and harnessing their unique characteristics.

The band gap, originally rooted in semiconductor physics, assumes a pivotal role in dictating how metamaterials engage with and govern waves, presenting unparalleled prospects for customizing their behavior across various applications. In conventional materials, the band gap typically denotes the energy range where electrons are prohibited, influencing the insulating or semiconducting traits of the material. In the domain of metamaterials, the concept of a band gap transcends its traditional electronic context to encompass the frequency range where electromagnetic or acoustic waves are forbidden. This distinctive attribute empowers metamaterials to selectively manage and filter waves based on their frequency. The capacity to precisely adjust the width and position of these band gaps provides versatile control over the interaction between metamaterials and waves. The appearance of band gaps, leading to significant attenuation within specific narrow frequency ranges, is especially intriguing. Consequently, there is considerable emphasis in the literature on the evaluation of these phenomena. Huang and Sun [6] explored dispersion curves and the band gap structure of a lattice system with multiple resonators arranged in a masses configuration connected by a spring. Their findings demonstrated that adjusting the spring constant and the internal masses' magnitude can shift the band gaps. Kumar and Pal [7] proposed a single-phase acoustic metamaterial featuring periodically arranged star-shaped units and conducted numerical simulations to characterize the band gaps. The results of the simulations revealed that the metamaterial possesses a continuous and extended band gap situated in the low-frequency range. In the work by Xia et al. [8], the acoustic transmission line method was introduced to examine the impact of water temperature on the local resonant band gap and the negative bulk modulus of an acoustic metamaterial. The results indicated that the relative variations in the local resonant band gap and the negative effective bulk modulus, influenced by changes in water temperature, are approximately equivalent and can reach up to about 11%. Reynolds and Daley [9] explore the primary properties of layered photonic periodic structures with photonic band gaps, including layers of backward-wave material, characterized by negative permittivity and permeability. In [10], they introduced a novel active viscoelastic metamaterial possessing a deep resonant band gap. The paper outlines a method developed to manipulate the band gap profile based on four key frequencies, demonstrating that coupling the natural frequency of the resonator and transmission units can change band gaps. Nobrega et al. [11] investigate band gaps in elastic metamaterial rods with spatial periodic distribution and periodically attached local resonators. They employ a modern methodology called the wave finite element method, developed for calculating dynamic behavior in periodic acoustic and structural systems. Nimmagadda and Matlack et al. [12] propose a method to thermally tune the band gaps of composite meta-structures, which combine a periodic lattice and locally resonant inclusions, through changes in the temperature of the structure. Dudek et al. [13] introduce a novel micro-scale mechanical metamaterial capable of transitioning between two configurations. One configuration exhibits a highly negative Poisson's ratio, indicative of strong auxeticity, while the other demonstrates a markedly positive Poisson's ratio. Ren and Liu [14] propose a groundbreaking active elastic metamaterial plate with tunable vibration band gap characteristics. This is achieved through the periodic placement of piezoelectric actuators and sensor pairs along one direction of the plate. Ning et al. [15] utilizes an elastomeric matrix with a square array of circular holes and resonating elements, including elastomeric coating and resonating mass, to design a new type of tunable acoustic metamaterial. Resonating elements are embedded into the elastomeric matrix, offering tunability in acoustic properties.

Inherently, band gaps are strictly related to the vibrational properties of the metamaterial structure, especially when they are subjected to external loads eventually leading to large displacements. Scientists and researchers have extensively investigated the vibrations of structures. Leissa [16–18] provided comprehensive classical plate and shell theories for various shapes and materials. Numerous authors have employed the free vibration method in their studies to assess dynamic properties under different loadings and boundary conditions. For instance, Tseng and Dugundji [19] analyzed the nonlinear vibration of a buckled beam, while Yamaki [20,21] investigated clamped beams subjected to bending. Lacarbonara et al. [22] conducted studies on the nonlinear vibrations of buckled beams, comparing analytical solutions with experimental results. Bhashyam and Prathap [23] utilized the Galerkin finite element method for nonlinear beam vibrations, highlighting key differences in eigenvalue problems between linear and nonlinear vibrations. Additional research in the realm of free vibration includes Fallah and Aghdam's [24] work on functionally graded beams and Asadi and Aghdam's [25] investigation into composite beams. Chen et al. [26] explored the nonlinear free vibration behavior of shear deformable sandwich porous beams within the context of Timoshenko beam theory. Ghasemi et al. [27] studied the free vibration of an orthotropic beam undergoing finite strain using Euler–Bernoulli beam governing equations. Mareishi et al. [28] delved into the nonlinear free vibration of laminated composite beams with surface-bonded piezoelectric fiber-reinforced composite layers under combined mechanical, thermal, and electrical loading, employing classical theories and von Kármán strains. Chandrashekhar and Ganguli [29] applied a third-order theory to conduct nonlinear vibration analyses of composite structures, evaluating the variance of natural frequencies due to randomness in material properties. Li and Qiao [30] recently presented geometrically nonlinear free vibration analysis of shear deformable anisotropic laminated composite beams resting on a two-parameter elastic foundation.

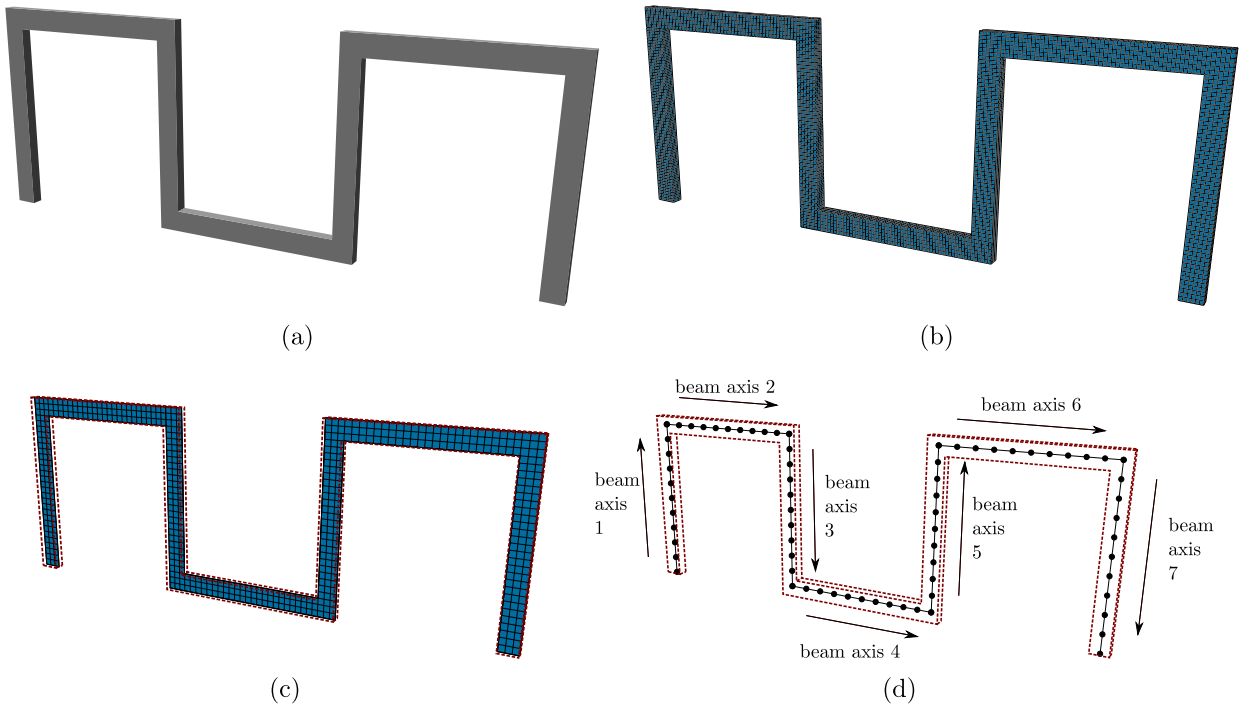


Fig. 1. Different approaches for the thin-walled structure made of repeatable cells (a), i.e. the use of 3D (b), 2D (c) and 1D (d) FEs.

The nonlinear analysis proposed in this study relies on the Carrera Unified Formulation (CUF) [31,32]. The CUF posits that any structural theory can be simplified into generalized kinematics, employing an arbitrary expansion of generalized variables. Consequently, the nonlinear governing equations and the corresponding finite element arrays for the generic geometrically exact beam theory are expressed in terms of fundamental nuclei. These nuclei serve as the fundamental building blocks that, when appropriately expanded, facilitate the straightforward generation of both low- and high-order finite beam elements. CUF has been successfully applied in numerous nonlinear engineering vibration problems [33,34].

This paper is organized as follows: (i) first, some preliminary and introductory information are given in Section 2, including the constitutive expressions for elastic metallic metamaterials, the Green–Lagrange nonlinear geometrical relations, CUF, and the related finite element; (ii) subsequently, Section 3 introduces the nonlinear problem and describes the fundamental nuclei of secant and tangent matrices. Moreover, it discusses the resolution of the nonlinear vibrations and explains the methodology applied in this work to investigate the evolution of the natural frequencies; (iii) then, numerical results are discussed for different structural cases in Section 4; (iv) finally, the main conclusions are drawn.

2. Refined one-dimensional finite element

2.1. One-dimensional mathematical model of metamaterials

The three-dimensional (3D) displacement field of a generic one-dimensional (1D) beam structure can be written in a vectorial form, and it reads:

$$\mathbf{u}(x, y, z) = \{u_x \; u_y \; u_z\}^T \tag{1}$$

where x, y and z are the coordinates of a Cartesian reference system. Assume that y is the direction of the beam axis, whereas x and z are the coordinates of the cross-section. The Carrera Unified Formulation (CUF) and the Finite Element Method (FEM) allows the 3D displacement field to be expressed as follows:

$$\mathbf{u}(x, y, z) = F_\tau(x, z) N_i(y) \mathbf{u}_{\tau i} \qquad \tau = 1, 2, \dots, M \qquad i = 1, 2, \dots, N_n \tag{2}$$

where $F_\tau(x, z)$ are the cross-section expansion functions in the x and z directions, where N_i stands for the ith shape function in the y direction, M represents the number of the terms used in the expansion, N_n stands for the number of the nodes on the beam axis and $\mathbf{u}_{\tau i}$ is the vector of the nodal unknowns. Lagrange Expansions (LE) are used as cross-sectional functions. They can ensure linear (L4), quadratic (L9), and cubic interpolation (L16), allowing the implementation of linear to higher-order kinematics. Carrera and Petrolo [35] provided more details about LE beam theories.

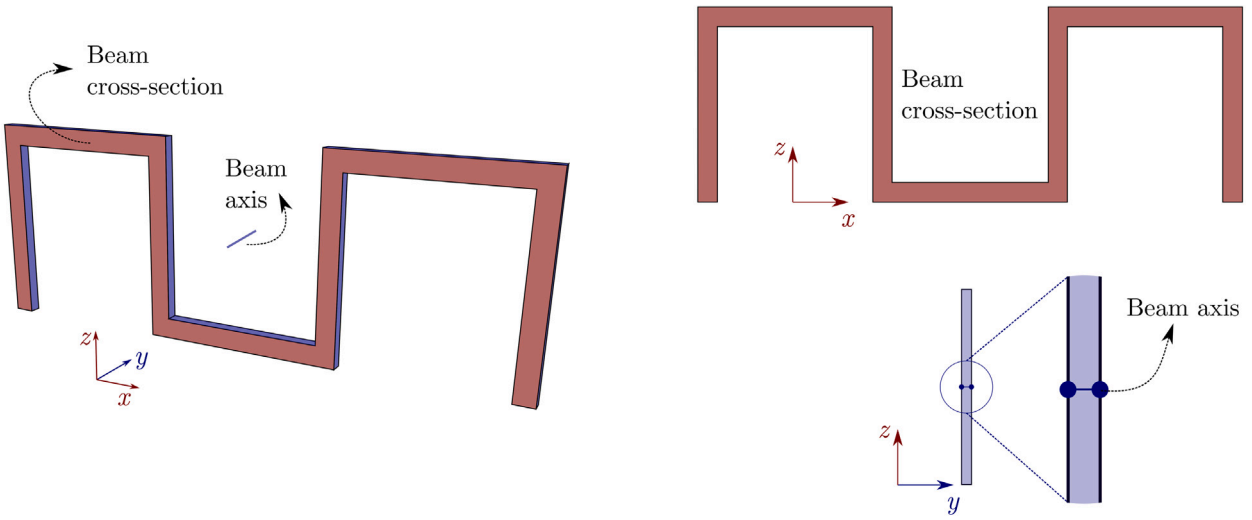


Fig. 2. Proposed mathematical modeling approach based on CUF.

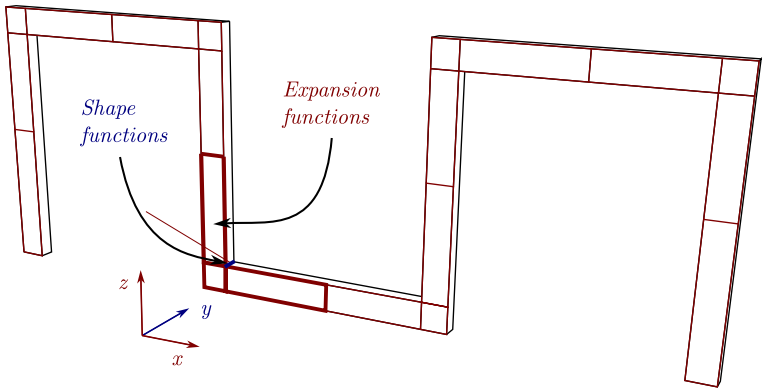


Fig. 3. Example of a metamaterial structure discretization.

Let us consider a thin-walled structure made of repeatable cells. Three types of modeling are ensured by commercial software. Fig. 1 shows them, i.e. the use of 3D, 2D and 1D Finite Elements (FEs). While the former stands out as the most accurate solution, it falls short in terms of computational efficiency. As emphasized in [36], a dependable through-thickness analysis requires the utilization of at least three to four solid elements. The thin nature of the components, coupled with the aspect ratio constraints inherent in 3D Finite Elements (FEs), results in a substantial number of degrees of freedom. Conversely, while opting for 2D Finite Elements (FEs) may seem reasonable given the slim profile of the structure, these elements lack the capacity to capture through-thickness strain and stress components, which can be pivotal from a design perspective. Similar conclusions apply to the final modeling approach involving 1D FEs. In this scenario, the structure is represented as multiple beams, typically relying on classical theories within commercial software. However, the drawbacks of classical theories, such as the omission of shear strain and lack of geometric exactitude, persist in this modeling technique. Moreover, they do not ensure that they are geometrically exact. Fig. 2 shows the proposed mathematical modeling approach based on CUF. In this instance, the structure is represented as a **single** beam. As illustrated in Fig. 2, the cross-section of the beam lies in the plane $x-z$ and is delineated in red, while the beam axis, depicted in blue, aligns with the direction y. The discretization of the cross-section is achieved using high-order Lagrange polynomials, enabling the accurate depiction of both local and global deformations and an exact representation of the geometry. This method allows for building models of very complex geometries, as depicted in Fig. 3, which would require the adoption of multiple-beam elements and effective methods for their connection with the conventional approach. With this approach, the displacement continuity between elements and sudden geometric changes are automatically ensured by the Lagrange points in common. Fig. 4 depicts this aspect of the proposed mathematical model.

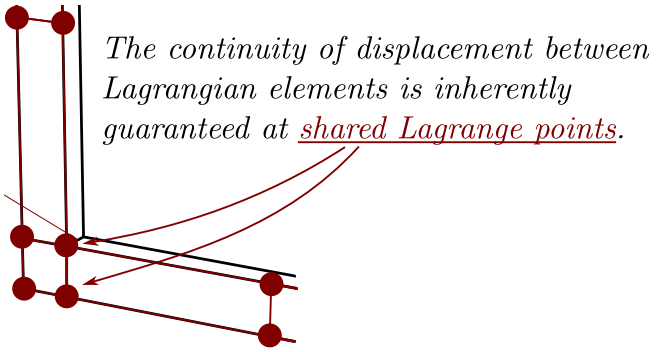


Fig. 4. Focus on Lagrange elements of a discretized metamaterial.

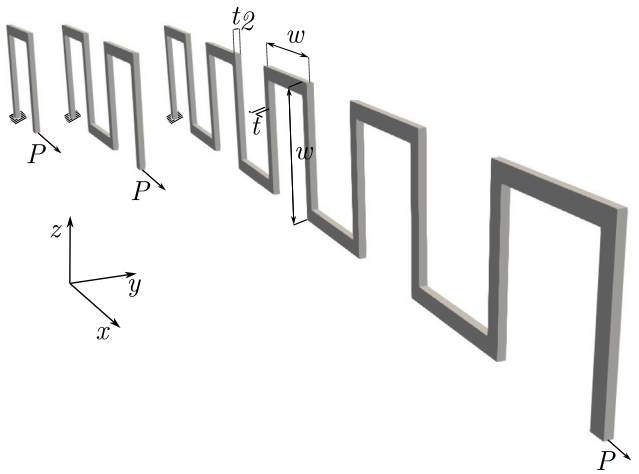


Fig. 5. Analyzed structures with repeatable cells. t = 10 mm and w = 100 mm.

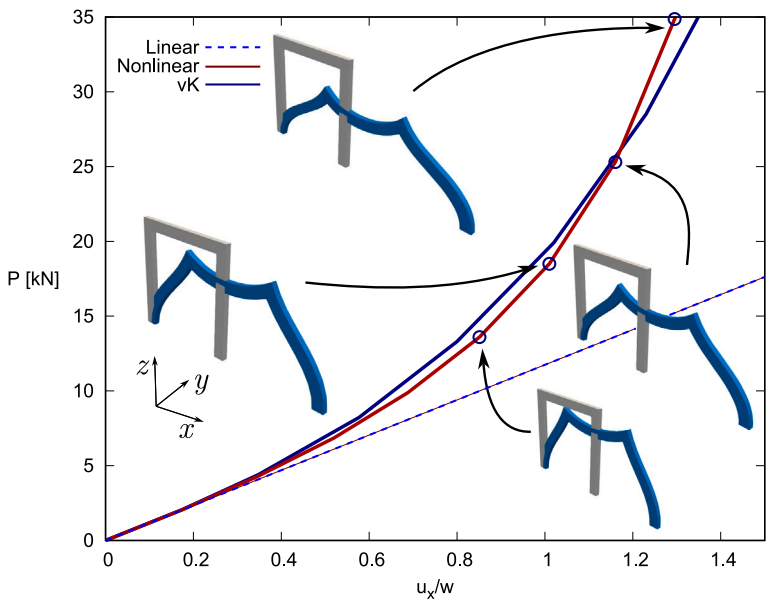


Fig. 6. Linear and nonlinear static curve of the one-cell structure. *Nonlinear* curve is evaluated using the full Green–Lagrange strain tensor, *vK* with the von Kármán nonlinearities. Depicted deformed configurations are at nonlinear equilibrium states.

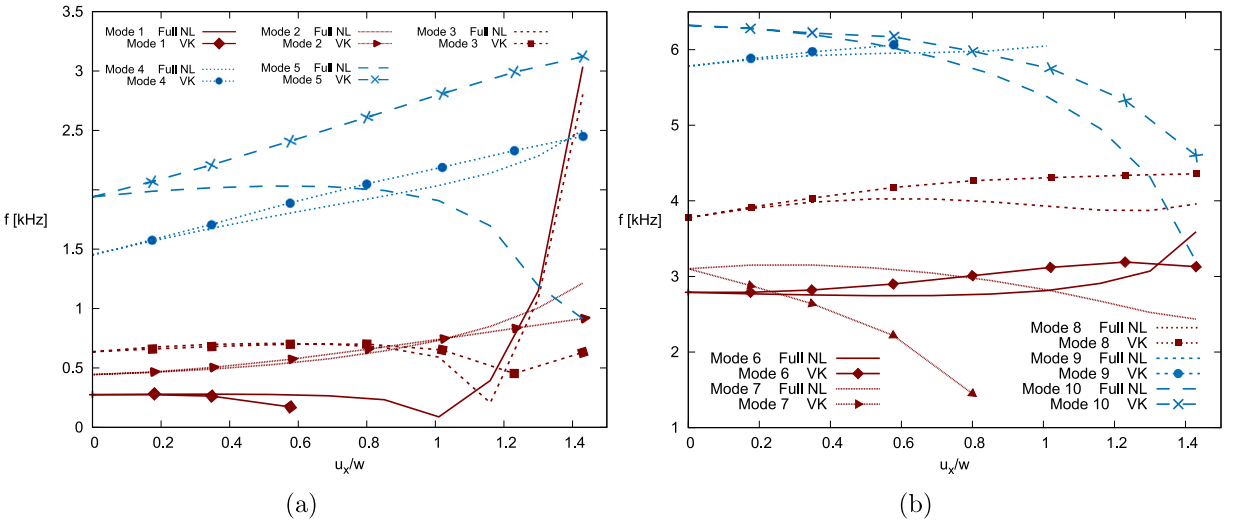


Fig. 7. Mode evolution of the one-cell structure, using linear (a) and nonlinear (b) stiffness matrix.

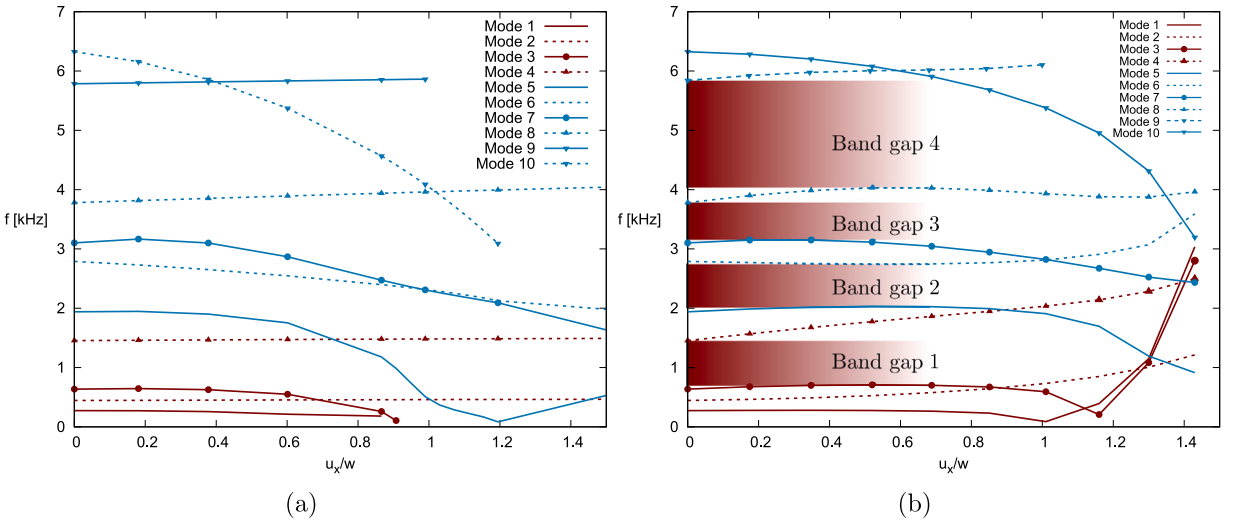


Fig. 8. Mode evolution of the one-cell structure, using linear (a) and nonlinear (b) stiffness matrix.

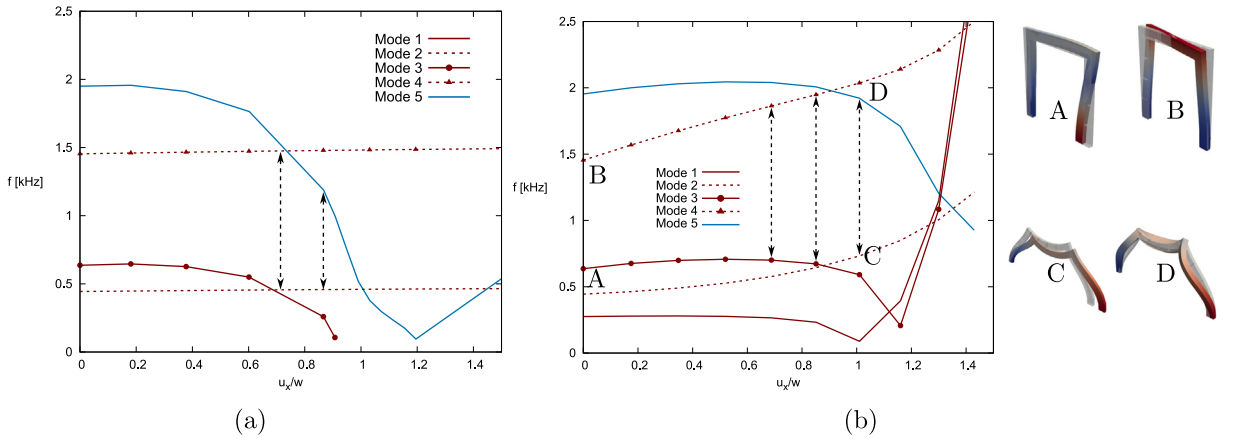


Fig. 9. First band gap evolution with linear (a) and nonlinear (b) stiffness matrix. One-cell structure case.

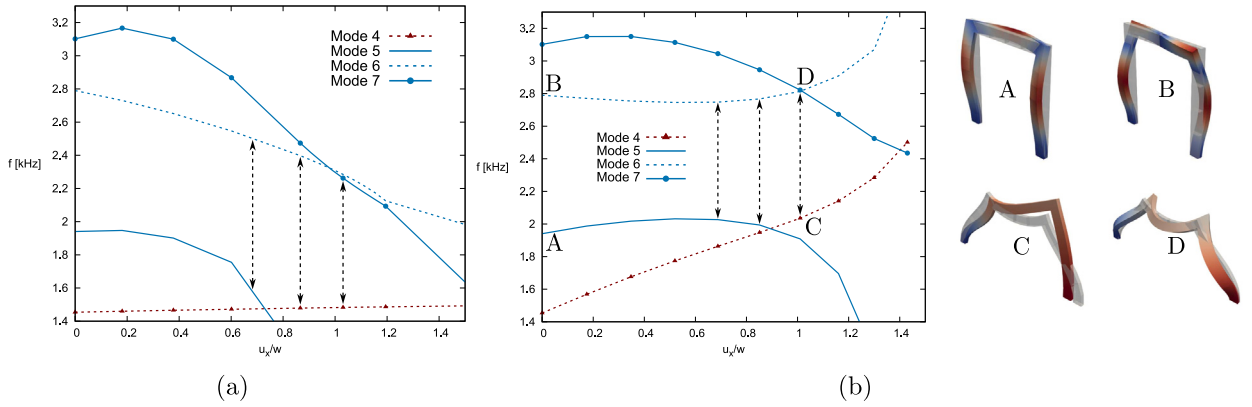


Fig. 10. Second band gap evolution with linear (a) and nonlinear (b) stiffness matrix. One-cell structure case.

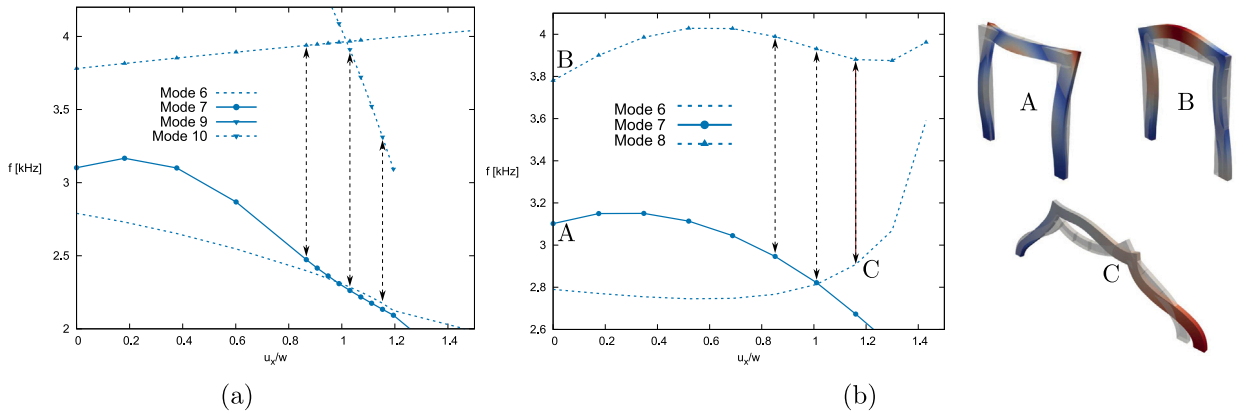


Fig. 11. Third band gap evolution with linear (a) and nonlinear (b) stiffness matrix. One-cell structure case.

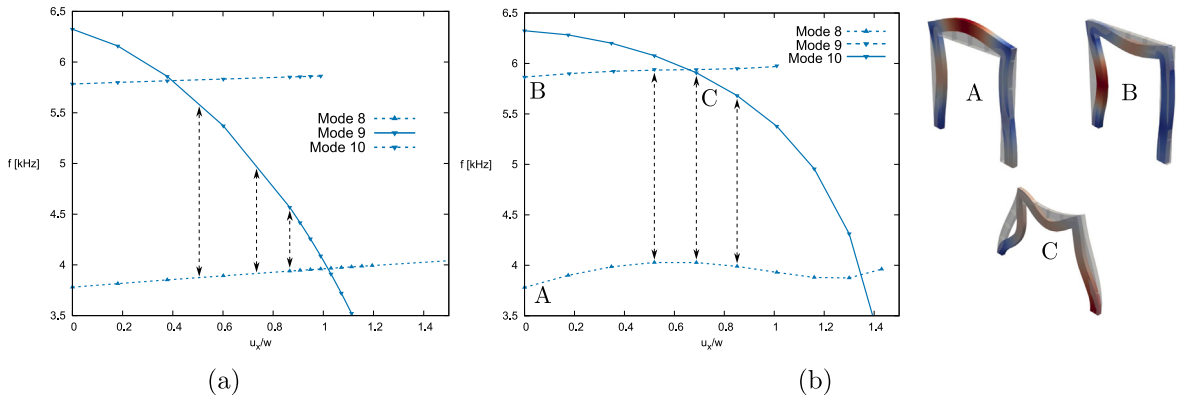


Fig. 12. Fourth band gap evolution with linear (a) and nonlinear (b) stiffness matrix. One-cell structure case.

2.2. Geometrical and constitutive relations

The stress, σ, and strain, ϵ, components are expressed in vectorial form with no loss of generality,

$$\begin{aligned}\sigma &= \{\sigma_{xx} \;\; \sigma_{yy} \;\; \sigma_{zz} \;\; \sigma_{xz} \;\; \sigma_{yz} \;\; \sigma_{xy}\}^T \\ \epsilon &= \{\epsilon_{xx} \;\; \epsilon_{yy} \;\; \epsilon_{zz} \;\; \epsilon_{xz} \;\; \epsilon_{yz} \;\; \epsilon_{xy}\}^T\end{aligned} \tag{3}$$

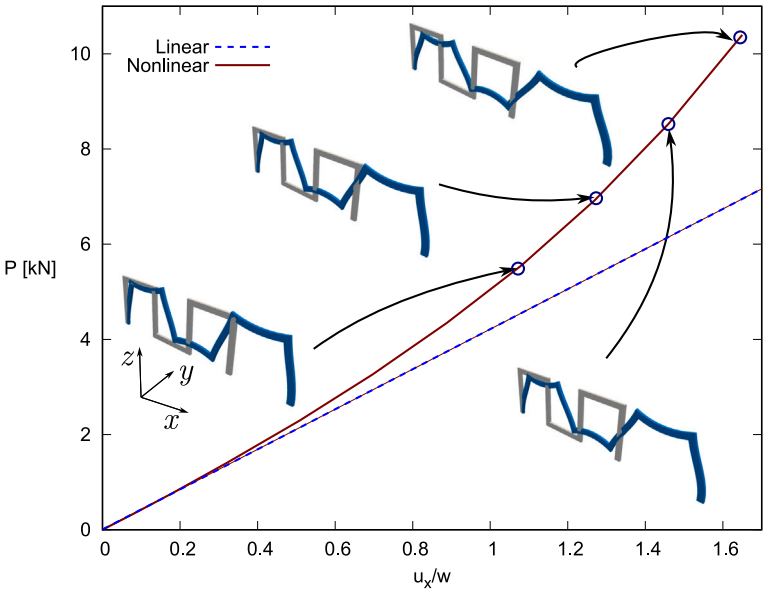


Fig. 13. Linear and nonlinear static curve of the two-cell structure. Depicted deformed configurations are at nonlinear equilibrium states.

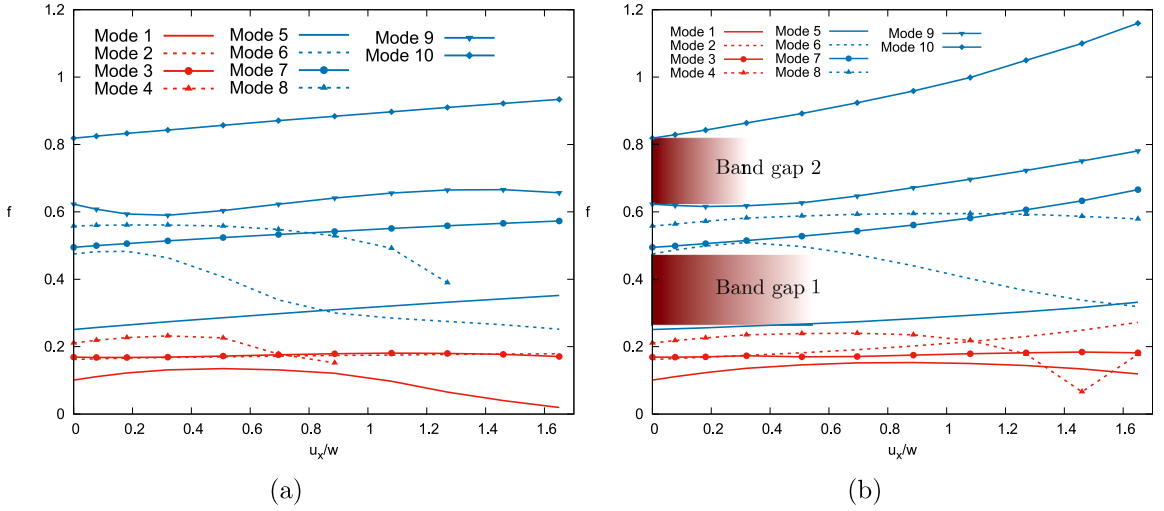


Fig. 14. Mode trend of the one-cell structure, using linear (a) and nonlinear (b) stiffness matrix.

As far as the geometrical relations are concerned, the Green–Lagrange nonlinear strain components are

$$\boldsymbol{\epsilon} = \boldsymbol{\epsilon}_l + \boldsymbol{\epsilon}_{nl} = (\mathbf{b}_l + \mathbf{b}_{nl})\mathbf{u}, \tag{4}$$

The 6×3 linear and nonlinear differential operators $\mathbf{b}_l$ and $\mathbf{b}_{nl}$ in Eq. (4) are given by:

$$\mathbf{b}_l = \begin{bmatrix} \partial_x & 0 & 0 \\ 0 & \partial_y & 0 \\ 0 & 0 & \partial_z \\ \partial_z & 0 & \partial_x \\ 0 & \partial_z & \partial_y \\ \partial_y & \partial_x & 0 \end{bmatrix}, \qquad \mathbf{b}_{nl} = \begin{bmatrix} \frac{1}{2}(\partial_x)^2 & \frac{1}{2}(\partial_x)^2 & \frac{1}{2}(\partial_x)^2 \\ \frac{1}{2}(\partial_y)^2 & \frac{1}{2}(\partial_y)^2 & \frac{1}{2}(\partial_y)^2 \\ \frac{1}{2}(\partial_z)^2 & \frac{1}{2}(\partial_z)^2 & \frac{1}{2}(\partial_z)^2 \\ \partial_x\partial_z & \partial_x\partial_z & \partial_x\partial_z \\ \partial_y\partial_z & \partial_y\partial_z & \partial_y\partial_z \\ \partial_x\partial_y & \partial_x\partial_y & \partial_x\partial_y \end{bmatrix} \tag{5}$$

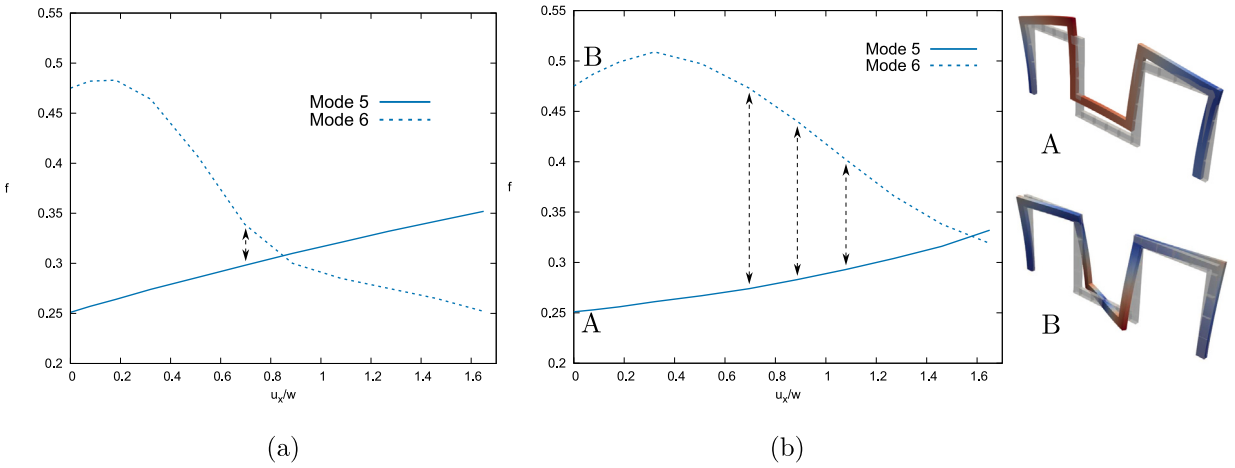


Fig. 15. First band gap evolution with linear (a) and nonlinear (b) stiffness matrix. Two-cell structure case.

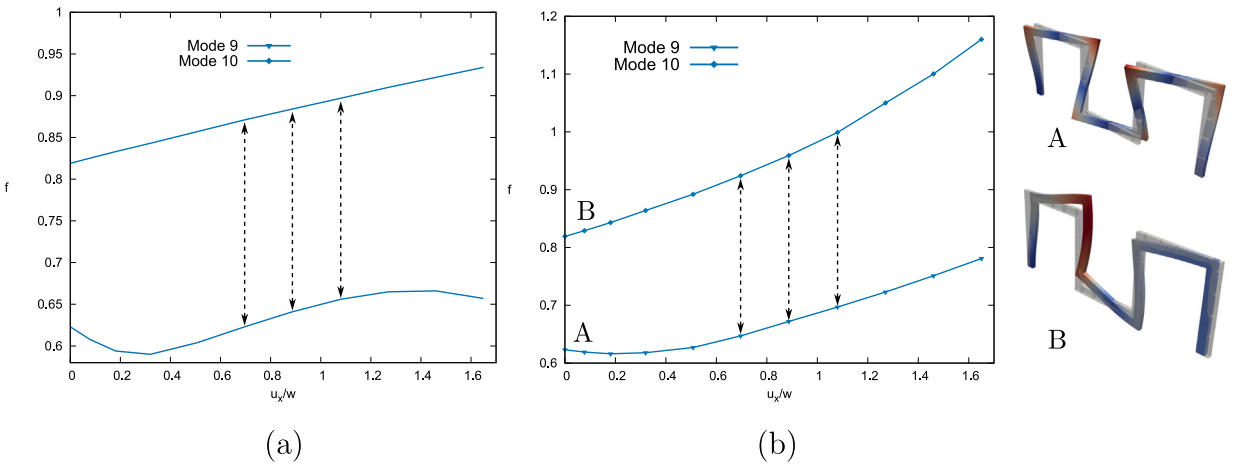


Fig. 16. Second band gap evolution with linear (a) and nonlinear (b) stiffness matrix. Two-cell structure case.

in which $\partial_\alpha = \partial(\cdot)/\partial\alpha$, $\partial_\beta = \partial(\cdot)/\partial\beta$, and $\partial_z = \partial(\cdot)/\partial z$. As far as the constitutive relation is concerned, linear elastic metallic shell structures are considered in this work. Consequently, the constitutive relation reads as:

$$\boldsymbol{\sigma} = \mathbf{C}\boldsymbol{\epsilon} \tag{6}$$

where C is the material elastic matrix, whose explicit form can be found in many books, see [37,38]. Finally, introducing the CUF and FEM relations into Eq. (4), the strain vector can be written in algebraic form as follows:

$$\boldsymbol{\epsilon} = (\mathbf{B}_l^{\tau i} + \mathbf{B}_{nl}^{\tau i})\mathbf{q}_{\tau i} \tag{7}$$

where $\mathbf{B}_l^{sj}$ and $\mathbf{B}_{nl}^{sj}$ are the linear and nonlinear algebraic matrices with CUF and FEM formulations. The explicit form of these two matrices is not reported here for the sake of brevity, but they are reported in [39].

3. Nonlinear free vibration

This section provides a brief introduction to vibration analysis. The principle of virtual displacements is recalled here, and it states that the virtual variation of the internal strain energy and the inertial forces is equal to the virtual variation of the external

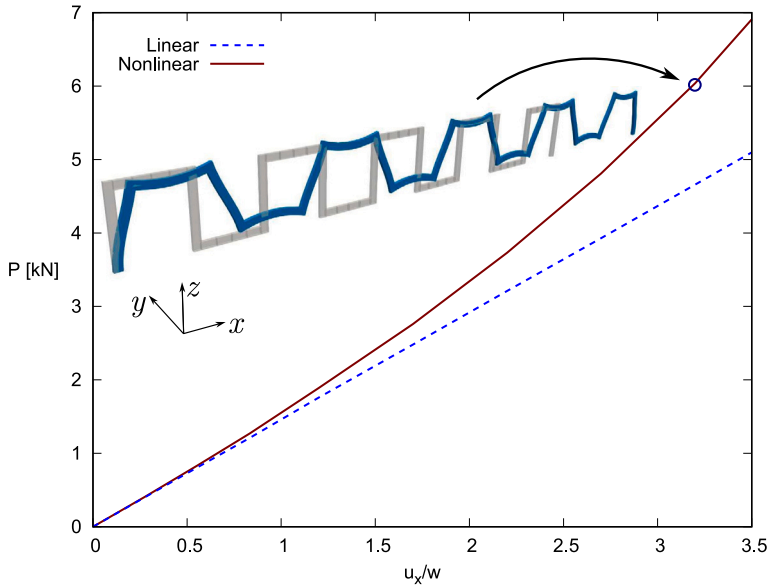


Fig. 17. Linear and nonlinear static curve of the five-cell structure. Depicted deformed configurations are at nonlinear equilibrium states.

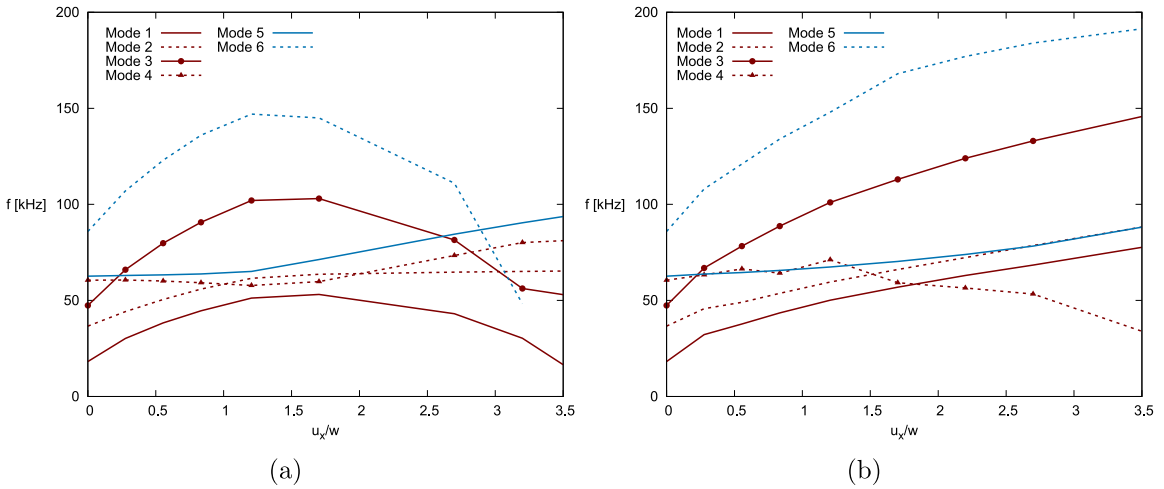


Fig. 18. Mode trend of the five-cell structure, using linear (a) and nonlinear (b) stiffness matrix.

forces. The virtual variation of the strain energy is formulated to derive the secant stiffness matrix $\mathbf{K}_S$. Specifically:

$$
\begin{aligned}
\delta L_{\text{int}} &= \delta \mathbf{q}_{sj}^T \int_\Omega (\mathbf{B}_l^{sj} + 2\mathbf{B}_{nl}^{sj})^T \boldsymbol{\sigma} \, \mathrm{dV} = \\
&= \delta \mathbf{q}_{sj}^T \int_\Omega (\mathbf{B}_l^{sj} + 2\mathbf{B}_{nl}^{sj})^T \mathbf{C} (\mathbf{B}_l^{\tau i} + \mathbf{B}_{nl}^{\tau i}) \, \mathrm{dV} \mathbf{q}_{\tau i} = \\
&= \delta \mathbf{q}_{sj}^T \mathbf{K}_0^{ij\tau s} \mathbf{q}_{\tau i} + \delta \mathbf{q}_{sj}^T \mathbf{K}_{lnl}^{ij\tau s} \mathbf{q}_{\tau i} \\
&+ \delta \mathbf{q}_{sj}^T \mathbf{K}_{nll}^{ij\tau s} \mathbf{q}_{\tau i} + \delta \mathbf{q}_{sj}^T \mathbf{K}_{nlnl}^{ij\tau s} \mathbf{q}_{\tau i} \\
&= \delta \mathbf{q}_{sj}^T \mathbf{K}_S^{ij\tau s} \mathbf{q}_{\tau i}
\end{aligned}
\tag{8}
$$

where $\mathbf{K}_0^{ij\tau s}$ is the linear contribution of $\mathbf{K}_S$ and $\mathbf{K}_{lnl}^{ij\tau s}$, $\mathbf{K}_{nll}^{ij\tau s}$, $\mathbf{K}_{nlnl}^{ij\tau s}$ indicate the nonlinear contributions. These components are expressed as CUF 3×3 Fundamental Nuclei (FNs). To enhance clarity, FNs serve as the fundamental building blocks of the presented theory. The FN remains independent of the theory approximation and can be expanded using the F_τ approximation (τ, $s = 1, \ldots, M$) and N_i shape functions (i, $j = 1, \ldots, N_n$). This expansion leads to the final stiffness matrix of any high-order model. The global stiffness matrix $\mathbf{K}_S$ is obtained by iterating over these indices. Employing the principle of virtual work, the virtual variations of

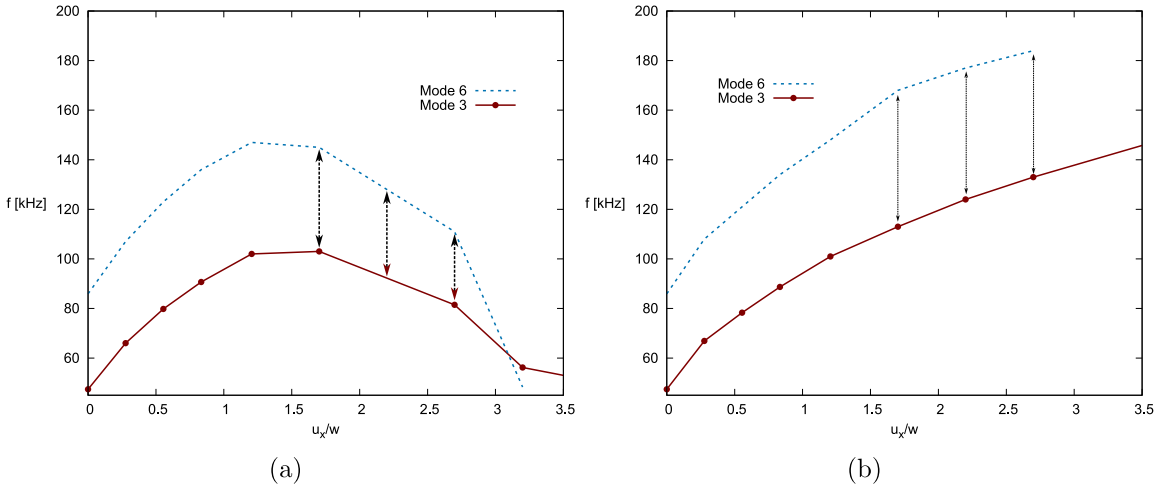


Fig. 19. Mode trend of the five-cell structure, using linear (a) and nonlinear (b) stiffness matrix.

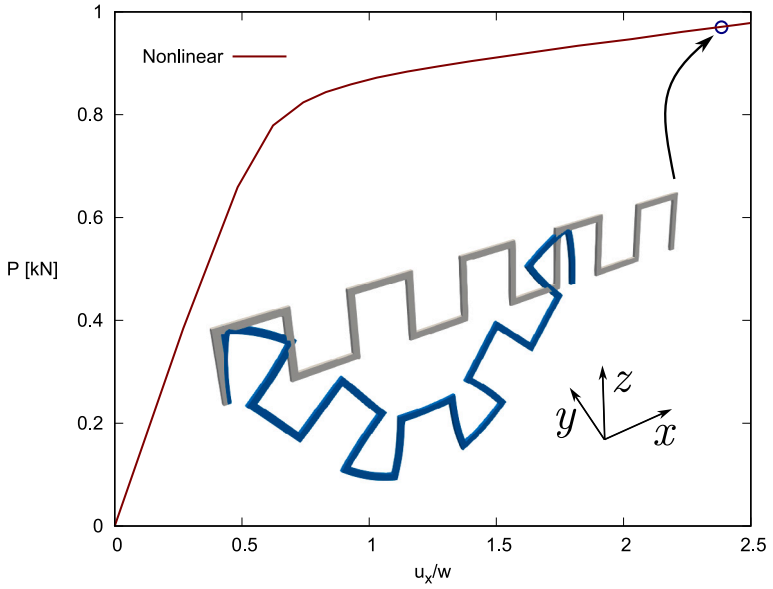


Fig. 20. Nonlinear static curve of the five-cell structure. Compression case.

internal and external work – where the latter is omitted here for brevity – are considered to establish the system of nonlinear equilibrium equations:

$$\mathbf{K}_S^{ij\tau s}\,\mathbf{q}_{\tau i} = \mathbf{p}_{sj} \tag{9}$$

Here, $\mathbf{p}_{sj}$ represents the FNs of the secant stiffness matrix and the vector of nodal loadings, respectively. These equations are solved using the Newton–Raphson method with the arc-length approach [40,41]. Similarly, the FNs of the mass matrix are derived from the virtual variation of the inertial loads:

$$\delta L_{\text{int}} = \delta \mathbf{q}_{sj}^T \mathbf{M}^{ij\tau s} \ddot{\mathbf{q}}_{\tau i} \tag{10}$$

in which $\mathbf{M}^{ij\tau s}$ represents the FN of the mass matrix and $\ddot{\mathbf{q}}_{\tau i}$ indicates the nodal acceleration vector; the dot stands for time derivative. As the modal behavior of a structure is not solely determined by its geometric and mechanical characteristics but is inherently tied to the state of equilibrium, eigenfrequencies and eigenmodes may experience sudden aberrations in deep nonlinear regimes [42]. To explore this aspect, vibration analysis is conducted around a linearized equilibrium state along the nonlinear path. Through the

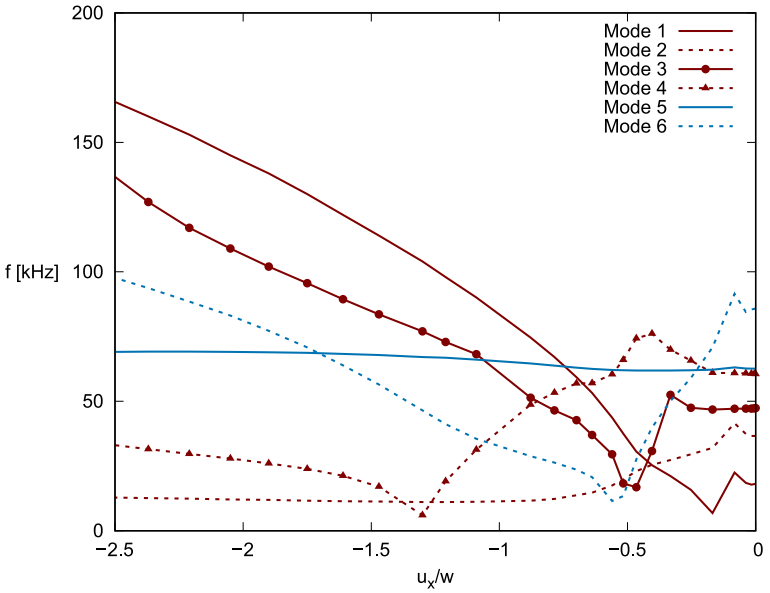


Fig. 21. Mode trend of the five-cell structure, using nonlinear stiffness matrix.

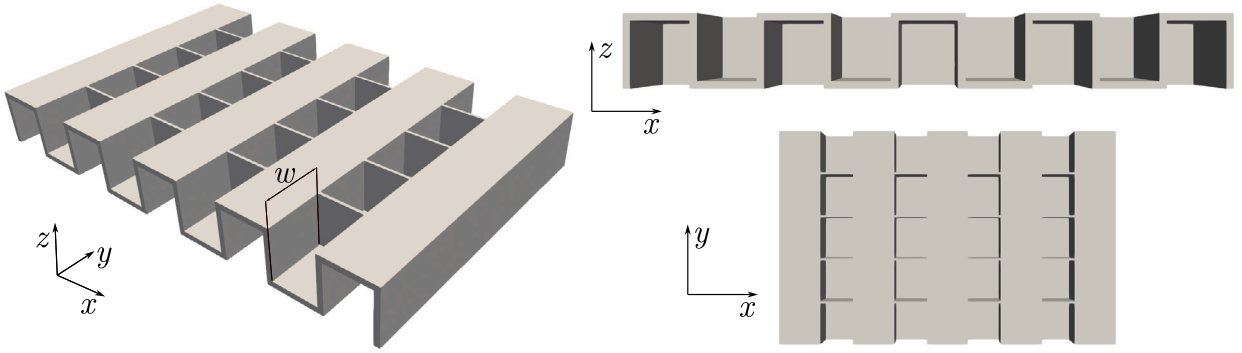


Fig. 22. Considered metamaterial structure. w = 100 mm.

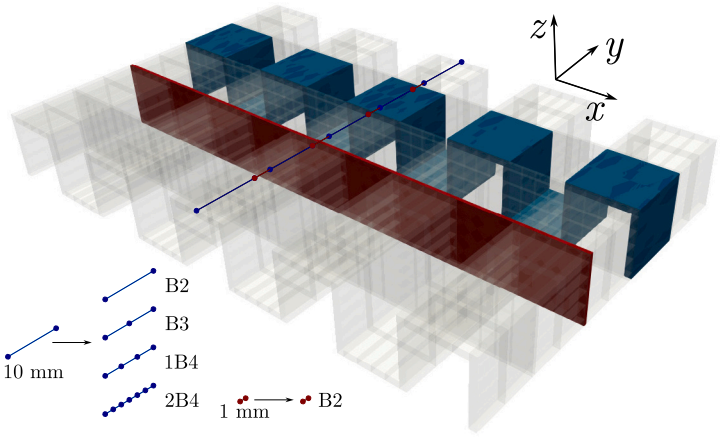


Fig. 23. Mathematical model of the metamaterial structure.

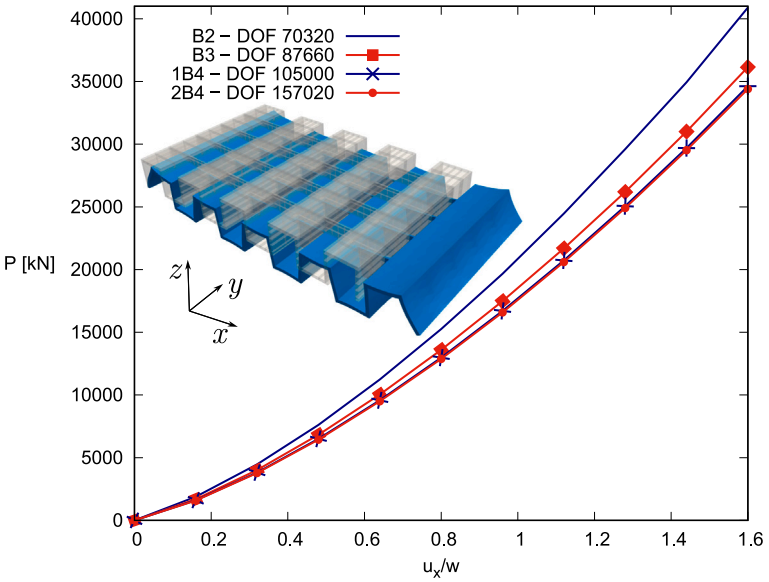


Fig. 24. Convergence analysis of the metamaterial structure under traction.

linearization of the virtual variation of the nonlinear strain energy, the tangent stiffness matrix ($\mathbf{K}_T$) is introduced.

$$\begin{aligned} &\delta(\delta L_{\text{int}} + \delta L_{\text{ine}} - \delta L_{\text{ext}}) \\ &\delta \mathbf{q}_{sj}^T (\mathbf{K}_0^{ij\tau s} + \mathbf{K}_{T1}^{ij\tau s}) \mathbf{q}_{\tau i} + \delta \mathbf{q}_{sj}^T \mathbf{K}_\sigma^{ij\tau s} \mathbf{q}_{\tau i} + \delta \mathbf{q}_{sj}^T \mathbf{M}^{ij\tau s} \ddot{\mathbf{q}}_{\tau i} \\ &\delta \mathbf{q}_{sj}^T \mathbf{K}_T^{ij\tau s} \mathbf{q}_{\tau i} + \delta \mathbf{q}_{sj}^T \mathbf{M}^{ij\tau s} \ddot{\mathbf{q}}_{\tau i} = 0 \end{aligned} \tag{11}$$

In deriving Eq. (11), it is assumed that the mass matrix is linear, and $\delta^2 L_{\text{ext}} = 0$ (loading is conservative). Here, $\mathbf{K}_T^{ij\tau s}$ represents the FN of the tangent stiffness matrix, $\mathbf{K}_0^{ij\tau s}$ indicates the linear component of $\mathbf{K}_T^{ij\tau s}$, $\mathbf{K}_{T1}^{ij\tau s} = 2\,\mathbf{K}_{lnl}^{ij\tau s} + \mathbf{K}_{nll}^{ij\tau s} + 2\,\mathbf{K}_{nlnl}^{ij\tau s}$ denotes the nonlinear contribution, and $\mathbf{K}_\sigma^{ij\tau s}$ is the geometric stiffness, a function of the linear ($\mathbf{K}_\sigma{}^{ij\tau s}$) and nonlinear ($\mathbf{K}_{\sigma_{nl}}{}^{ij\tau s}$) pre-stress state, where:

$$\sigma = \sigma_l + \sigma_{nl} = \mathbf{C}(\epsilon_l + \epsilon_{nl}) \tag{12}$$

Finally, the full global stiffness matrices are obtained by assembling the FNs versus the indexes τ, $s = 1, \ldots, \text{M}$ and $i, j = 1, \ldots, p+1$. For more details about the expansion of the FNs and the finite element assembly procedure in the framework of CUF, the readers are referred to Carrera et al. [32].

The displacement variations in Eq. (11) are considered small, allowing for the assumption of harmonic vibration. Consequently, the system can be solved as a linear eigenvalue problem. In summary, vibrations around nonlinear equilibrium states can be conducted as follows:

- Initially, the static geometrical nonlinear problem is resolved using the Newton–Raphson method based on the arc-length approach.
- Subsequently, after computing the nonlinear equilibrium curve, the tangent stiffness matrix is determined at each state of interest.
- Following this, by taking into account the incremental linearized equilibrium condition of Eq. (11) and assuming harmonic motion around nontrivial equilibrium states,

$$\begin{aligned} \delta \mathbf{q}_{\tau i}(t) &= \delta \tilde{\mathbf{q}}_{\tau i} e^{i\omega t} \\ \delta \ddot{\mathbf{q}}_{\tau i}(t) &= -\omega^2 \delta \tilde{\mathbf{q}}_{\tau i} e^{i\omega t} \end{aligned} \tag{13}$$

The equations of motion are simplified into a linear eigenvalue problem, allowing the evaluation of natural frequencies and mode shapes:

$$(\mathbf{K}_T^{ij\tau s} - \omega^2 \mathbf{M}^{ij\tau s}) \tilde{\mathbf{q}}_{\tau i} e^{i\omega t} = 0 \tag{14}$$

Here, ω represents the natural frequency, and $\tilde{\mathbf{q}}_{\tau i}$ is the eigenvector. Additionally, for clarity, it is crucial to emphasize that the nonlinear vibrations exhibit low amplitudes, and small increments of amplitudes are considered when determining the nonlinear vibration modes. Consequently, it is legitimate to employ linearization around the state of equilibrium for problem resolution.

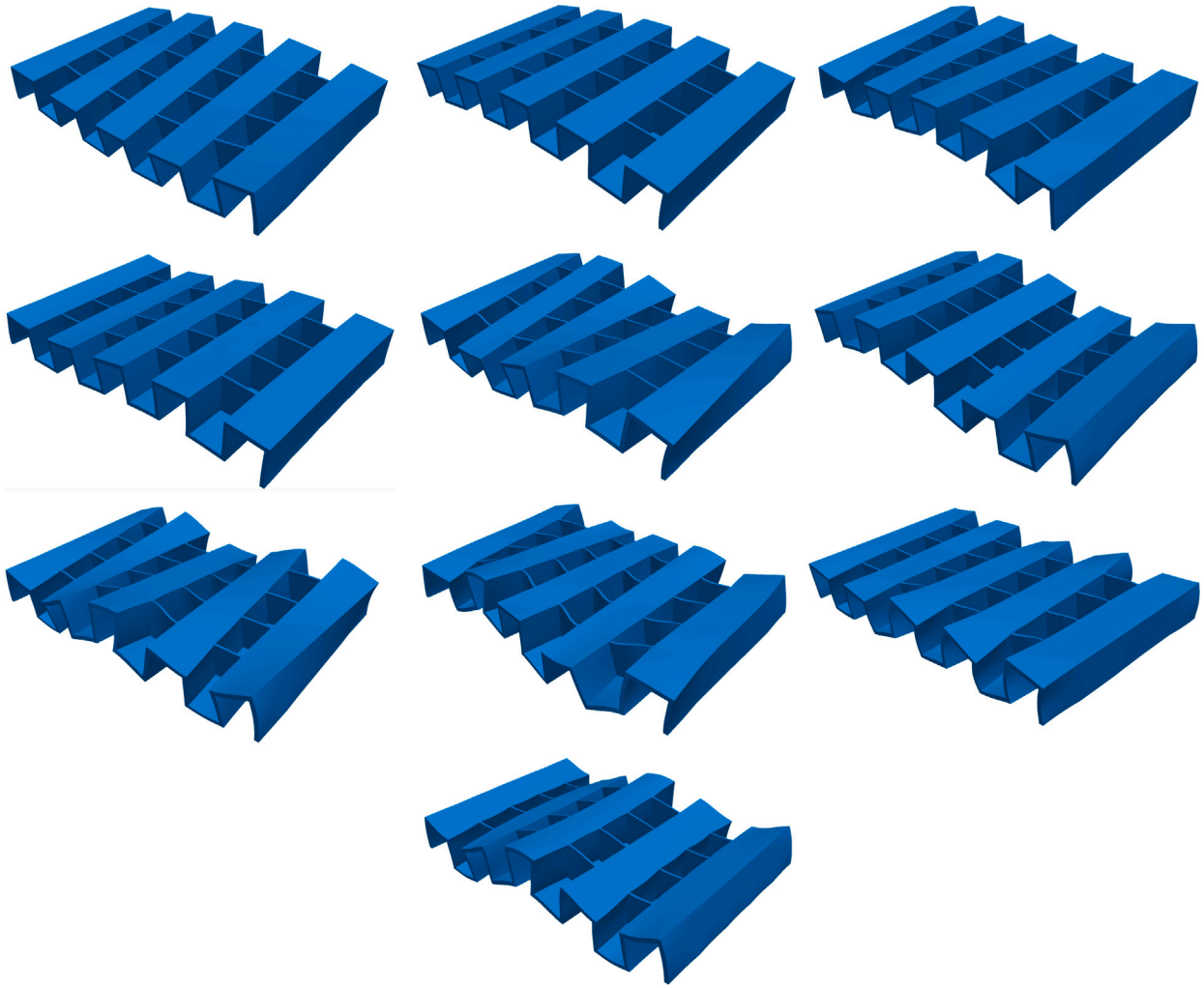


Fig. 25. The first ten modes of the unloaded metamaterial structure.

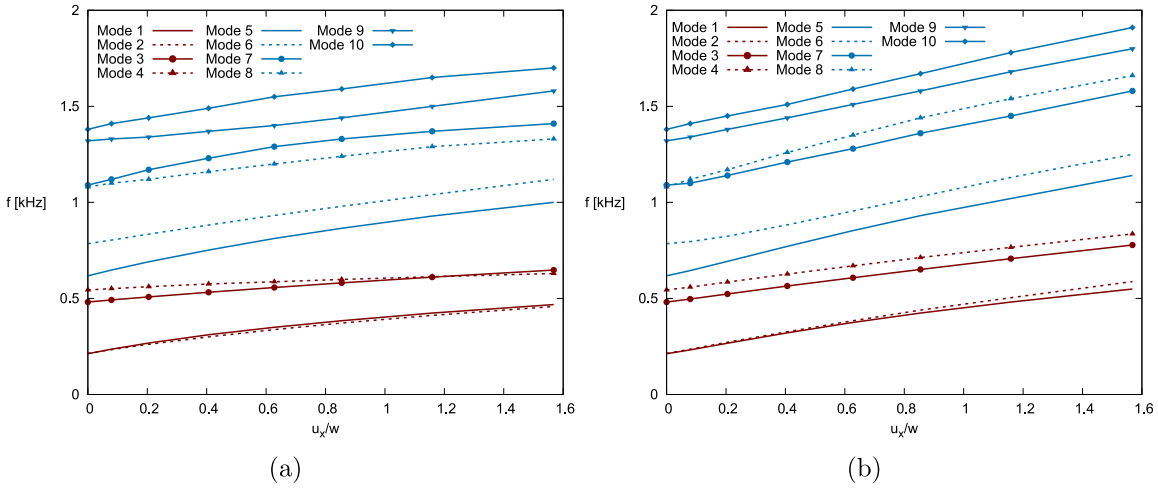


Fig. 26. Mode trend of the metamaterial structure, using linear (a) and nonlinear (b) stiffness matrix.

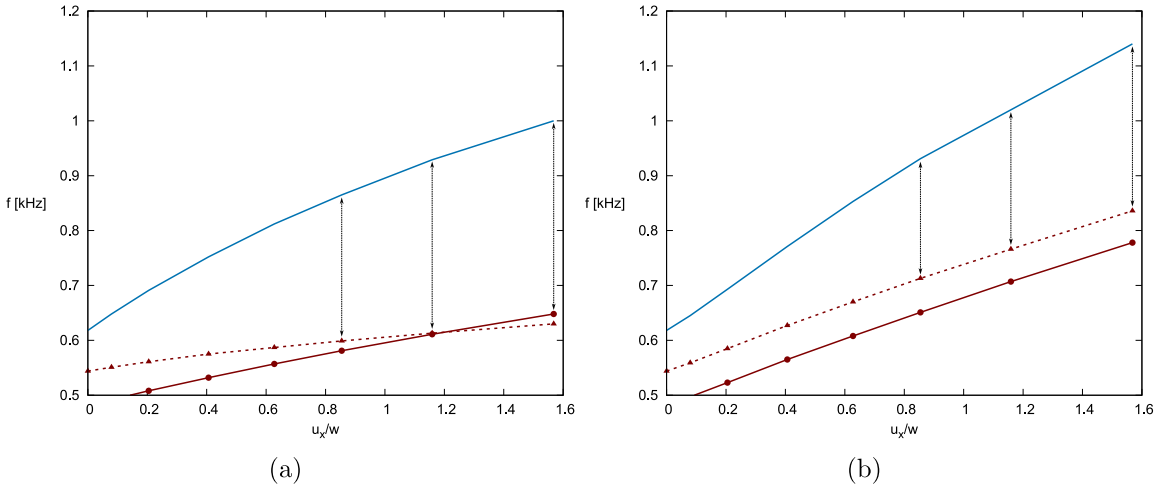


Fig. 27. Mode trend of the five-cell structure, using linear (a) and nonlinear (b) stiffness matrix.

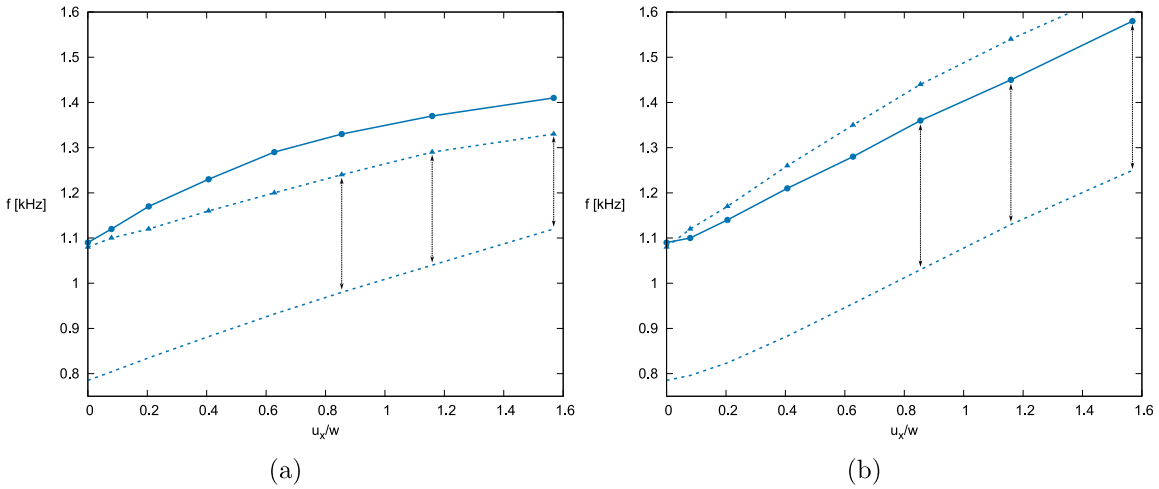


Fig. 28. Mode trend of the five-cell structure, using linear (a) and nonlinear (b) stiffness matrix.

Usually, a resolution based on a linear approach is standard in most literature. Therefore, this work emphasizes the comparison between linear and nonlinear approaches, highlighting the necessity of adopting a complete nonlinear formulation for accurate analyses. Through linearization around the trivial equilibrium state, the tangent stiffness matrix is expressed as:

$$\mathbf{K}_T = \mathbf{K}_0 + \lambda \mathbf{K}_{\sigma l} \tag{15}$$

Here, λ represents the progressively increasing load factor. This simplified linearized approach is executed by substituting Eq. (15) into Eq. (11), wherein $\mathbf{K}_{T1}$ tends to zero due to the small values of δu.

4. Numerical results

The provided numerical findings pertain to metamaterial structures featuring repeatable cells. The geometric characteristics are sourced from [43], where the analysis focused on the nonlinear static equilibrium. In the cited study, a thorough comparison was conducted between the suggested mathematical model and those derived using solid finite elements, emphasizing the decrease in required degrees of freedom. Additionally, a convergence analysis was performed, and the current work utilizes the same chosen models. Illustrated in Fig. 5 are structures with dimensions of $t = 10$ mm and $w = 100$ mm. These encompass one-cell, two-cell, and five-cell configurations. An in-plane traction loading condition is imposed on one end, while the structures are clamped on the opposite side. Furthermore, the behavior of the five-cell case is examined under compression loading conditions. Finally, the case of a more complicated metamaterial-like structure is proposed.

Table 1
Values of frequency limits of the one-cell structure case band gaps. Frequencies expressed in [kHz]. f_{lin} stands for frequency evaluated using linear stiffness matrix, f_{nl} using nonlinear stiffness matrix. % range diff. is the percentage difference between the band gaps evaluated using linear and nonlinear stiffness matrix.

Band gap	u_x/w	$f_{1_{lin}}^{n\ mode} - f_{2_{lin}}^{n\ mode}$	$f_{1_{nl}}^{n\ mode} - f_{2_{nl}}^{n\ mode}$	% range diff.
1 Fig. 9	0.69	$0.454^3 - 1.479^4$	$0.700^3 - 1.863^4$	12%
	0.85	$0.458^3 - 1.179^4$	$0.672^3 - 1.947^4$	43%
	1.01	–	$0.732^2 - 1.909^5$	–
2 Fig. 10	0.69	$1.755^5 - 2.547^6$	$2.027^5 - 2.747^6$	−10%
	0.85	$1.479^4 - 2.398^6$	$1.994^5 - 2.767^6$	−19%
	1.01	$1.483^4 - 2.262^7$	$2.035^4 - 2.812^7$	0%
3 Fig. 11	0.85	$2.473^7 - 3.893^8$	$2.946^7 - 3.989^8$	−36%
	1.01	$2.398^6 - 3.910^{10}$	$2.823^7 - 3.931^8$	−36%
	1.16	$2.134^6 - 3.313^{10}$	$2.908^6 - 3.880^8$	−21%
4 Fig. 12	0.52	$3.852^8 - 5.622^{10}$	$4.028^8 - 5.948^9$	8%
	0.69	$3.893^8 - 5.372^{10}$	$4.027^8 - 5.908^{10}$	21%
	0.85	$3.939^8 - 4.568^{10}$	$3.989^8 - 5.682^{10}$	63%

4.1. One-cell structure

The first case is the one-cell structure of Fig. 5. The nonlinear equilibrium curve, showcasing the response to a traction force P, is depicted in Fig. 6, accompanied by selected far full nonlinear deformed configurations. The assessment also includes the examination of the curve with von Kármán nonlinearities (see [44] for details about the von Kármán nonlinearities modeling in the CUF framework). Clear distinctions are observable among the three curves, encompassing variations between the complete nonlinear curve and those incorporating von Kármán nonlinearities. Those distinctions are more evident in Fig. 7, where the mode evaluation between the full nonlinear and the von Kármán solutions are presented. Therefore, utilizing the complete nonlinear matrix is essential and will be employed for all subsequent analyses, referred to as the *nonlinear* configuration.

The natural frequencies are assessed at various equilibrium states. This process is executed for both linear and nonlinear solutions, and the corresponding outcomes are presented in Fig. 8. The first ten frequencies are computed, and in Fig. 8, each curve corresponds to a distinct mode shape.

Evidently, four distinct band gaps emerge from the mode distribution, and each is individually examined, comparing the linear and nonlinear solutions. Focusing on the first band gap, detailed in Fig. 9, three values of u_x/w, namely 0.69, 0.85, and 1.01, are considered. In the linear solution, the band gap diminishes as u_x/w increases, disappearing entirely at $u_x/w = 1.01$. Additionally, within the nonlinear domain, the band gap is situated between modes 3 and 4 for $u_x/w = 0.69$ and 0.85, whereas it shifts to modes 2 and 5 for $u_x/w = 1.01$. This shift results from mode alterations and aberrations in the nonlinear field. The corresponding mode shapes in the nonlinear field are presented in the same figure.

The progression of the second band gap is depicted in Fig. 10. The same values of u_x/w are considered, highlighting noticeable distinctions between linear and nonlinear solutions. In the linear scenario, the band gap transitions from modes 5–6 to modes 4–6 and then to modes 4–7. Conversely, in the nonlinear case, it spans from modes 5–6 for $u_x/w = 0.69, 0.85$ to modes 4–7 for $u_x/w = 1.01$. For the latter case, the mode shapes on the deformed configurations are provided. Moreover, Fig. 11 illustrates the distribution of the third band gap. The pattern closely mirrors the evolution of the second band gap. In this instance, the linear solution describes a band gap shift different from the nonlinear case. The values $u_x/w = 0.85, 1.01$ and 1.16 are examined to assess the band gaps, and the corresponding deformed configurations are presented.

In conclusion, the fourth band gap is illustrated in Fig. 12, considering $u_x/w = 0.52, 0.69$ and 0.85. The frequencies corresponding to the previously examined band gaps are provided in Table 1. The substantial difference in range between the linear and nonlinear solutions is significant and cannot be overlooked. Consequently, it is imperative to incorporate the nonlinear stiffness matrix in the assessment of band gaps within the large displacement field.

4.2. Two-cell structure

This section covers the scenario of the two-cell structure, with the geometry illustrated in Fig. 6. The static equilibrium curves for linear and nonlinear cases are presented in Fig. 13. Additionally, four deformed configurations are provided. Similar to the previous case, the distribution of the first mode over the in-plane displacement is illustrated, and the results are displayed in Fig. 14. In this instance, the focus is on the two primary band gaps, as illustrated in Fig. 14(b). The details of the first band gap are presented in Fig. 15. Three values of u_x/w are examined, namely 0.70, 0.89, and 1.08. It is noteworthy that the band gaps predicted by the linear approach disappear for $u_x/w = 0.89, 1.08$. For $u_x/w = 0.70$, the difference between the linear and nonlinear solutions is substantial, reaching almost 80%, as indicated in Table 2, which provides the band gap values for the two-cell structure case. The transition of the second band gap is illustrated in Fig. 16. Notably, in this instance, the band gaps calculated by the linear and nonlinear approaches closely align, as reflected in the values in Table 2.

Table 2
Values of frequency limits of the two-cell structure case band gaps. Frequencies expressed in [kHz]. f_{lin} stands for frequency evaluated using linear stiffness matrix, f_{nl} using nonlinear stiffness matrix. % range diff. is the percentage difference between the band gaps evaluated using linear and nonlinear stiffness matrix.

Band gap	u_x/w	$f_{1\,lin}^{n\,mode} - f_{2\,lin}^{n\,mode}$	$f_{1\,nl}^{n\,mode} - f_{2\,nl}^{n\,mode}$	% range diff.
1 Fig. 15	0.70	$0.298^5 - 0.339^6$	$0.274^5 - 0.473^6$	79%
	0.89	–	$0.283^5 - 0.440^6$	–
	1.08	–	$0.293^5 - 0.402^6$	–
2 Fig. 16	0.70	$0.623^9 - 2.547^{10}$	$0.647^9 - 0.924^{10}$	−10%
	0.89	$0.641^9 - 2.398^{10}$	$0.672^9 - 0.959^{10}$	−19%
	1.08	$0.656^9 - 2.262^{10}$	$0.697^9 - 0.999^{10}$	0%

Table 3
Values of frequency limits of the five-cell structure case band gaps. Frequencies expressed in [kHz]. f_{lin} stands for frequency evaluated using linear stiffness matrix, f_{nl} using nonlinear stiffness matrix. % range diff. is the percentage difference between the band gaps evaluated using linear and nonlinear stiffness matrix.

Band gap	u_x/w	$f_{1\,lin}^{n\,mode} - f_{2\,lin}^{n\,mode}$	$f_{1\,nl}^{n\,mode} - f_{2\,nl}^{n\,mode}$	% range diff.
Fig. 16	1.70	$0.103^3 - 0.145^6$	$0.133^3 - 0.168^6$	−20%
	2.20	$0.097^3 - 0.123^6$	$0.124^3 - 0.177^6$	51%
	2.70	$0.082^3 - 0.111^6$	$0.113^3 - 0.184^6$	47%

4.3. Five-cell structure — traction

This section proposed the results of the band gap evaluation of the five-cell structure. Fig. 17 shows the linear and nonlinear static behavior of this structure. The deformed configuration at $u_x = 3.2$ is reported in the same figure. Fig. 18 reports the mode change of such structure, including the first six modes. The band gap between modes 3 and 6 is analyzed hereafter and the related frequency values are reported in Table 3. Clearly, this band gap arises from both linear and nonlinear solutions for $u_x = 2.2, 2.7$ and 3.2, and it remains between modes 3 and 6. However, as underlined by Table 3, the % difference between the two band gaps is high, especially in the far nonlinear regime, reaching values of 51% and 47% for $u_x = 2.2$ and 2.7, respectively (see Fig. 19).

4.4. Five-cell structure — compression

This study examines the response of a five-cell structure under compressive loading conditions. The nonlinear static curve can be observed in Fig. 20, along with a representation of the deformed configuration in the far nonlinear regime. Fig. 21 illustrates the distributions of the first six modes concerning the negative displacements at the structure's tip. Notably, there are evident shifts and deviations in mode behavior. The evolution of band gaps is apparent, reinforcing the previous findings, i.e. the necessity of incorporating the nonlinear stiffness matrix in modal analysis.

4.5. Metamaterial structure

The concluding case study revolves around a metamaterial structure that shares the same cross-section and mathematical discretization as the structure outlined in Section 4.3. Furthermore, this structure is strengthened by the addition of four evenly spaced transverse stiffeners, as illustrated in Fig. 22. Fig. 23 illustrates the mathematical model of the structure. The transverse stiffeners, highlighted in red, have a width of 10 mm and are discretized using a linear finite element, identified as B2 in the figure. Additionally, the blue segments of the structure are represented using B2 elements, quadratic elements denoted as B3, and cubic elements denoted as B4. Utilizing each mathematical model, nonlinear static analysis under traction is conducted, maintaining the same boundary conditions as in the preceding numerical cases. The outcomes of these analyses are presented in Fig. 24. It is evident that the 1B4 configuration (refer to Fig. 23) can be regarded as a converged model, making it the chosen one for the evaluation of the band gap. The first ten modes of the unloaded metamaterial structure, i.e. $u_x/w = 0$ are depicted in Fig. 25. The first ten modes are then evaluated in correspondence of the equilibrium states on the linear and nonlinear patch of the structure. The results are reported in Fig. 26. The shift in mode frequencies is evident, particularly the exchange between modes 8 and 9, a phenomenon observed in the linear case but not in the nonlinear scenario. The considered band gaps are those at 0.6 and 1 kHz, which are depicted in Figs. 27 and 28, respectively, and the related numerical values are reported in Table 4. In the context of the first band gap, as the u_x/w ratio increases, the disparity in the range diminishes from −30% to −15%. However, the edge frequencies exhibit an increasing discrepancy, with values of 0.649 kHz to 1.000 kHz and 0.836 kHz to 1.140 kHz for $u_x/w = 1.57$. Conversely, within the second band gap, the range difference experiences an augmentation, reaching its maximum value of 52% when $u_x/w = 1.57$. In summary, the disparities between the linear and nonlinear cases are conspicuous, consistently with the findings of prior numerical examinations. Hence, a nonlinear analysis is imperative for an accurate band gap assessment.

Table 4
Values of frequency limits of the metamaterial structure case band gaps. Frequencies expressed in [kHz]. f_{lin} stands for frequency evaluated using linear stiffness matrix, f_{nl} using nonlinear stiffness matrix. % range diff. is the percentage difference between the band gaps evaluated using linear and nonlinear stiffness matrix.

Band gap	u_x/w	$f_{1_{lin}}^{n\ mode} - f_{2_{lin}}^{n\ mode}$	$f_{1_{nl}}^{n\ mode} - f_{2_{nl}}^{n\ mode}$	% range diff.
1 Fig. 26	0.85	$0.581^3 - 0.865^5$	$0.713^4 - 0.931^5$	−30%
	1.16	$0.613^4 - 0.929^5$	$0.766^4 - 1.020^5$	−24%
	1.57	$0.649^3 - 1.000^5$	$0.836^4 - 1.140^5$	−15%
2 Fig. 27	0.85	$0.980^6 - 1.328^7$	$1.031^6 - 1.358^8$	−6%
	1.16	$1.042^6 - 1.366^7$	$1.127^6 - 1.454^8$	27%
	1.57	$1.116^6 - 1.407^7$	$1.254^6 - 1.576^8$	52%

5. Conclusions

This study delved into the dynamic behavior of metamaterials, exploring the evolution of their band gap within the large displacement/rotations field. The research employed a unified model based on the Carrera Unified Formulation (CUF), facilitating the development of higher-order one-dimensional beam theories capable of accounting of geometric nonlinearities via cross-sectional expansion functions, whereas the discretization of the axis was achieved through a finite element approximation. Equations of motion were solved around nonlinear static equilibrium states in a total Lagrangian scenario, identified through the utilization of a Newton–Raphson algorithm in conjunction with a path-following method of arc-length type. Notably, the paper conducted a detailed comparison of results obtained with both linear and nonlinear stiffness matrices, elucidating the distinctions between them. Numerical investigations were conducted on thin-walled structures comprised of repeatable cells, allowing for the assessment of mode changes under traction and compression loading conditions. The results clearly show that the adoption of the full Green–Lagrange strain tensor is mandatory. In addition to these analyses, the paper introduced a more intricate metamaterial-like structure. The findings underscored the inherent nature of the band gap as a property of the equilibrium state, accentuating the imperative need for a thorough nonlinear analysis to evaluate frequency transitions precisely.

CRediT authorship contribution statement

R. Augello: Writing – review & editing, Writing – original draft, Investigation. **E. Carrera:** Writing – review & editing, Writing – original draft, Supervision, Methodology, Investigation, Conceptualization.

Declaration of competing interest

The authors declare that they have no known competing financial interests or personal relationships that could have appeared to influence the work reported in this paper.

Data availability

No data was used for the research described in the article.

References

[1] D.R. Smith, N. Kroll, Negative refractive index in left-handed materials, Phys. Rev. Lett. 85 (14) (2000) 2933.
[2] V.G. Vesselago, The electrodynamics of substances with simultaneously negative values of permittivity and permeability, Sov. Phys. Uspekhi 10 (4) (1968) 509–514.
[3] N. Fang, D. Xi, J. Xu, M. Ambati, W. Srituravanich, C. Sun, X. Zhang, Ultrasonic metamaterials with negative modulus, Nat. Mater. 5 (6) (2006) 452–456.
[4] H. Chen, C.T. Chan, Acoustic cloaking and transformation acoustics, J. Phys. D: Appl. Phys. 43 (11) (2010) 113001.
[5] Z. Liu, X. Zhang, Y. Mao, Y.Y. Zhu, Z. Yang, C.T. Chan, P. Sheng, Locally resonant sonic materials, Science 289 (5485) (2000) 1734–1736.
[6] G.L. Huang, C.T. Sun, Band gaps in a multiresonator acoustic metamaterial, J. Vib. Acoust. 132 (3) (2010) 031003.
[7] N. Kumar, S. Pal, Low frequency and wide band gap metamaterial with divergent shaped star units: Numerical and experimental investigations, Appl. Phys. Lett. 115 (25) (2019).
[8] B. Xia, N. Chen, L. Xie, Y. Qin, D. Yu, Temperature-controlled tunable acoustic metamaterial with active band gap and negative bulk modulus, Appl. Acoust. 112 (2016) 1–9.
[9] I.S. Nefedov, S.A. Tretyakov, Photonic band gap structure containing metamaterial with negative permittivity and permeability, Phys. Rev. E 66 (3) (2002) 036611.
[10] M. Reynolds, S. Daley, Enhancing the band gap of an active metamaterial, J. Vib. Control 23 (11) (2017) 1782–1791.
[11] E.D. Nobrega, F. Gautier, A. Pelat, J.M.C. Dos Santos, Vibration band gaps for elastic metamaterial rods using wave finite element method, Mech. Syst. Signal Process. 79 (2016) 192–202.
[12] C. Nimmagadda, K.H. Matlack, Thermally tunable band gaps in architected metamaterial structures, J. Sound Vib. 439 (2019) 29–42.
[13] K.K. Dudek, J.A. Iglesias Martínez, G. Ulliac, L. Hirsinger, L. Wang, V. Laude, M. Kadic, Micro-scale mechanical metamaterial with a controllable transition in the Poisson's ratio and band gap formation, Adv. Mater. (2023) 2210993.
[14] T. Ren, C. Liu, F. Li, C. Zhang, Active tunability of band gaps for a novel elastic metamaterial plate, Acta Mech. 231 (2020) 4035–4053.
[15] S. Ning, F. Yang, C. Luo, Z. Liu, Z. Zhuang, Low-frequency tunable locally resonant band gaps in acoustic metamaterials through large deformation, Extreme Mech. Lett. 35 (2020) 100623.

[16] A.W. Leissa, Vibration of Plates, vol. 160, Scientific and Technical Information Division, National Aeronautics and Space Administration, 1969.
[17] A.W. Leissa, Vibration of Shells, vol. 288, Scientific and Technical Information Office, National Aeronautics and Space Administration, 1973.
[18] A.W. Leissa, M.S. Qatu, Vibrations of Continuous Systems, McGraw-Hill Education, 2011.
[19] W.-Y. Tseng, J. Dugundji, Nonlinear Vibrations of a Buckled Beam Under Harmonic Excitation, J. Appl. Mech. 38 (2) (1971) 467–476.
[20] N. Yamaki, A. Mori, Non-linear vibrations of a clamped beam with initial deflection and initial axial displacement, part I: theory, J. Sound Vib. 71 (3) (1980) 333–346.
[21] N. Yamaki, K. Otomo, A. Mori, Non-linear vibrations of a clamped beam with initial deflection and initial axial displacement, Part II: Experiment, J. Sound Vib. 71 (3) (1980) 347–360.
[22] W. Lacarbonara, A.H. Nayfeh, W. Kreider, Experimental validation of reduction methods for nonlinear vibrations of distributed-parameter systems: analysis of a buckled beam, Nonlinear Dynam. 17 (1998) 95–117.
[23] G.R. Bhashyam, G. Prathap, Galerkin finite element method for non-linear beam vibrations, J. Sound Vib. 72 (2) (1980) 191–203.
[24] A. Fallah, M.M. Aghdam, Nonlinear free vibration and post-buckling analysis of functionally graded beams on nonlinear elastic foundation, Eur. J. Mech. A Solids 30 (4) (2011) 571–583.
[25] H. Asadi, M.M. Aghdam, Large amplitude vibration and post-buckling analysis of variable cross-section composite beams on nonlinear elastic foundation, Int. J. Mech. Sci. 79 (2014) 47–55.
[26] D. Chen, S. Kitipornchai, J. Yang, Nonlinear free vibration of shear deformable sandwich beam with a functionally graded porous core, Thin-Walled Struct. 107 (2016) 39–48.
[27] A.R. Ghasemi, F. Taheri-Behrooz, S.M.N. Farahani, M. Mohandes, Nonlinear free vibration of an Euler-Bernoulli composite beam undergoing finite strain subjected to different boundary conditions, J. Vib. Control 22 (3) (2016) 799–811.
[28] S. Mareishi, M. Rafiee, X.Q. He, K.M. Liew, Nonlinear free vibration, postbuckling and nonlinear static deflection of piezoelectric fiber-reinforced laminated composite beams, Composites B 59 (2014) 123–132.
[29] M. Chandrashekhar, R. Ganguli, Nonlinear vibration analysis of composite laminated and sandwich plates with random material properties, Int. J. Mech. Sci. 52 (7) (2010) 874–891.
[30] Z.-M. Li, P. Qiao, On an exact bending curvature model for nonlinear free vibration analysis shear deformable anisotropic laminated beams, Compos. Struct. 108 (2014) 243–258.
[31] E. Carrera, G. Giunta, M. Petrolo, Beam Structures: Classical and Advanced Theories, John Wiley & Sons, 2011.
[32] E. Carrera, M. Cinefra, M. Petrolo, E. Zappino, Finite Element Analysis of Structures Through Unified Formulation, John Wiley & Sons, 2014.
[33] A. Pagani, R. Augello, E. Carrera, Frequency and mode change in the large deflection and post-buckling of compact and thin-walled beams, J. Sound Vib. 432 (2018) 88–104.
[34] E. Carrera, A. Pagani, R. Augello, Effect of large displacements on the linearized vibration of composite beams, Int. J. Non-Linear Mech. 120 (2020) 103390.
[35] E. Carrera, M. Petrolo, Refined beam elements with only displacement variables and plate/shell capabilities, Meccanica 47 (2012) 537–556.
[36] A.G. De Miguel, I. Kaleel, M.H. Nagaraj, A. Pagani, M. Petrolo, E. Carrera, Accurate evaluation of failure indices of composite layered structures via various FE models, Compos. Sci. Technol. 167 (2018) 174–189.
[37] K.-J. Bathe, Finite Element Procedures, Klaus-Jurgen Bathe, 2006.
[38] T.J.R. Hughes, The Finite Element Method: Linear Static and Dynamic Finite Element Analysis, Courier Corporation, 2012.
[39] A. Pagani, E. Carrera, Unified formulation of geometrically nonlinear refined beam theories, Mech. Adv. Mater. Struct. 25 (1) (2018) 15–31.
[40] M. Crisfield, An arc-length method including line searches and accelerations, Internat. J. Numer. Methods Engrg. 19 (9) (1983) 1269–1289.
[41] E. Carrera, A study on arc-length-type methods and their operation failures illustrated by a simple model, Comput. Struct. 50 (2) (1994) 217–229.
[42] G. Kerschen, Modal Analysis of Nonlinear Mechanical Systems, vol. 555, Springer, 2014.
[43] E. Carrera, A. Pagani, D. Giusa, R. Augello, Nonlinear analysis of thin-walled beams with highly deformable sections, Int. J. Non-Linear Mech. 128 (2021) 103613.
[44] A. Pagani, E. Carrera, R. Augello, Evaluation of various geometrical nonlinearities in the response of beams and shells, AIAA J. 57 (8) (2019) 3524–3533.